

PARTICLE TRAPPING AND STREAMING INSTABILITY IN VORTICES IN PROTOPLANETARY DISKS

NATALIE RAETTIG¹, HUBERT KLAHR¹, AND WLADIMIR LYRA^{2,3,4}¹Max-Planck-Institut für Astronomie, Königstuhl 17, D-69117, Heidelberg, Germany; raettig@mpia.de, klahr@mpia.de²Division of Geological & Planetary Science, California Institute of Technology, 1200 E California Blvd MC 150-12, Pasadena, CA 91125, USA³Jet Propulsion Laboratory, California Institute of Technology, 4800 Oak Grove Drive, Pasadena, CA 91109, USA; wlyra@caltech.edu

Received 2013 August 12; accepted 2014 November 22; published 2015 April 28

ABSTRACT

We analyze the concentration of solid particles in vortices created and sustained by radial buoyancy in protoplanetary disks, e.g., baroclinic vortex growth. Besides the gas drag acting on particles, we also allow for back-reaction from dust onto the gas. This becomes important when the local dust-to-gas ratio approaches unity. In our two-dimensional, local, shearing sheet simulations, we see high concentrations of grains inside the vortices for a broad range of Stokes numbers, St . An initial dust-to-gas ratio of 1:100 can easily be reversed to 100:1 for $St = 1.0$. The increased dust-to-gas ratio triggers the streaming instability, thus counter-intuitively limiting the maximal achievable overdensities. We find that particle trapping inside vortices opens the possibility for gravity assisted planetesimal formation even for small particles ($St = 0.01$) and a low initial dust-to-gas ratio of $1:10^4$, e.g., much smaller than in the previously studied magnetohydrodynamic zonal flow case.

Key words: accretion, accretion disks – hydrodynamics – instabilities – methods: numerical – turbulence

1. INTRODUCTION

A quantitative prescription of planetesimal formation is one of the key issues of planet formation theory. Models of simple collisional sticking are controversially discussed, both conceptually and also in the explanation of current properties of asteroid and Kuiper Belt objects (Bottke et al. 2005; Morbidelli et al. 2009; Nesvorný et al. 2011; Weidenschilling 2011). Whether small dust grains stick to one another, bounce, or fragment depends on their size and their relative velocities. In general, theory predicts that collisional velocities rise as particles grow, which holds for particles with a Stokes number smaller than one, e.g., meter sized objects at 5 AU. Both drift velocity and turbulence-induced relative velocities have a maximum when the stopping time of an object (τ_r) is of the order of an orbital period ($1/\Omega$), which leads to the Stokes number $St = \Omega\tau_r = 1$ (see, e.g., the review by Weidenschilling & Cuzzi 1993). Fragmentation occurs at velocities of only a few ms^{-1} , which limits particle sizes to millimeters-centimeters (Wurm & Blum 2000; Brauer et al. 2008; Birnstiel et al. 2010). Güttler et al. (2010) and Zsom et al. (2010) introduced another boundary, the so-called bouncing barrier where particles hit one another and bounce without mass transfer. At even smaller size scales, Okuzumi et al. (2011a, 2011b) found the charge barrier, where small particles are prevented from approaching one another due to the electric charges built up through collisions with free electrons. Birnstiel et al. (2012) determined the sizes that particles can obtain locally as their growth is limited by radial drift and collisional destructions. They find, almost independently of the distance from the star, a maximum Stokes number of about 0.01–0.1 which corresponds to 1–10 cm at 1 AU, 0.3 – 3 cm at 10 AU, and 0.3–3 mm at 100 AU (see Figures 5 and 6 in Birnstiel et al. 2012).

To form large planetesimals, these difficulties need to be circumvented. One proposed method is gravitational instability (Safronov 1972; Goldreich & Ward 1973; Johansen et al. 2006a, 2007, 2011). When a sufficient amount of particles is close enough together, their mutual attraction can

trigger gravitational collapse, rapidly forming large planetesimals that then sweep up small particles (Lambrechts & Johansen 2012). Different methods to capture dust have been studied, such as zonal flows by Johansen et al. (2011) and Dittrich et al. (2013), pressure rings around stars (Whipple 1972; Klahr & Lin 2001, 2005), convection cells (Klahr & Henning 1997), or vortices, either numerically (Tanga et al. 1996; Johansen et al. 2004; Lyra et al. 2008a, 2009a, 2009b; Meheut et al. 2012b) or analytically (Barge & Sommeria 1995; Chavanis 2000; Klahr & Bodenheimer 2006; Chang & Oishi 2010; Lyra & Lin 2013).

From these studies, it has become clear that dust can easily concentrate in anticyclonic vortices. However, besides, e.g., Lyra et al. (2009a) and Meheut et al. (2012b) who analyzed vortices excited by the Rossby Wave Instability, other studies did not choose a particular formation mechanism for vortices. Feedback of dust on the gas flow in vortices has not been studied in detail and is the topic of this study. In our study, vortices are naturally produced by the radial stratification of disks (Klahr & Bodenheimer 2003; Petersen et al. 2007a, 2007b; Lesur & Papaloizou 2010; Lyra & Klahr 2011; Raettig et al. 2013). The growth of the vortices occurs proportionally to the radial buoyancy frequency (a.k.a. Brunt–Väisälä frequency), squared N^2 (Raettig et al. 2013), and the local thermal relaxation timescale, as argued by Lesur & Papaloizou (2010) and numerically confirmed by Raettig et al. (2013). The buoyancy frequency, which is a function of the relative scale height H/r , logarithmic radial entropy and pressure gradients β_K , β_P , and the adiabatic index γ :

$$N^2 = -\frac{1}{\gamma} \left(\frac{H}{r} \right)^2 \beta_K \beta_P. \quad (1)$$

A linear theory to explain this behavior has been put forward by Klahr & Hubbard (2014) who identify the instability as a radial “convective overstability” in accretion disks. Lyra (2014) performed 3D simulations of this “convective overstability” and showed that in the nonlinear phase vortices were indeed emerging from the flow.

⁴ Sagan Fellow.

In this paper, we want to find out how efficiently dust can be concentrated in vortices enforced by realistic values for the radial stratification in temperature and density with a plausible value for the thermal relaxation time. We do this as a first step via two-dimensional (2D), local simulations. Ultimately, only three-dimensional (3D) stratified runs will be able to include all relevant physics from vortex stability (Barranco & Marcus 2005; Lesur & Papaloizou 2009; Lyra & Klahr 2011) to sedimentation of dust, yet are beyond technical feasibility for the scope of this paper.

Nevertheless, we find that, even in 2D sufficiently high particle concentration in the vortices, the back-reaction of the particles onto the gas must be considered in our simulations. We find that the streaming instability (Youdin & Goodman 2005; Johansen et al. 2006a) is triggered, counter-intuitively limiting the maximum dust-to-gas ratio and severely perturbing the gas flow inside the vortex. In some cases, we see vortices getting disrupted that later reform, starting a new concentration cycle of particles.

In simulations similar to ours, but 3D and more numerically expensive, where particles were trapped in zonal flows of magnetohydrodynamical origin and including self-gravity, the overdensities that we found in the present paper already lead to a gravitational collapse (Johansen et al. 2006b, 2007) and to the formation of planetesimals. On the other hand, 2D simulations including particle feedback are ideally suited to study a wide parameter range to learn whether streaming instability can be triggered and how it affects the stability of the vortices.

The paper is structured as follows. We first review the underlying physics of dust-motion in a gas disk, specifically in a vortex including dust-gas interactions. Then we describe the numerical setup. The results of our simulations are given in Section 4. Here we especially look at the reached dust-to-gas ratios compared to the average initial dust-to-gas ratio. In Section 5, we discuss the prospects of forming planetesimals via the gravitational fragmentation of dust enhancements in vortices and, in Section 6, we present our measurements of collisional speeds among dust grains. Finally, we summarize and conclude in Section 7.

2. PHYSICAL BACKGROUND

The evolution of the gas component of the disk in the Pencil Code is given by the Navier–Stokes equation containing stellar gravity as well as the virtual forces of the rotating and shearing box as explicit terms (Lyra & Klahr 2011). Dust grains on the other hand are evolved by solving the equations of motion for Lagrangian particles (see Section 3).

In general, the gas and dust experience the same external forces except for the pressure force $f_p = -\rho_g^{-1} \nabla p$, where ρ_g is the gas density and p the pressure. This term only affects the gas. For instance, the global pressure gradient in the gas leads to a sub-Keplerian orbital gas velocity \mathbf{u} . The corresponding buoyancy force for a particle is $f_{p,s} = -\rho_s^{-1} \nabla p$, where ρ_s is the material density of the solid material and can be neglected because $\rho_s \gg \rho_g$. Since the particles do not experience this global pressure, they need to orbit at Keplerian velocities in order to be in centrifugal balance with stellar gravity. The resulting velocity difference between gas and large particles acts as a headwind on the particles, which decreases their angular momentum leading to radial drift inward. Smaller

particles get dragged along by the gas and, therefore, feel a net acceleration toward the star also making them drift inward.

The time on which the dust particles adjust to the gas velocity is the friction time. For subsonic Epstein drag, this is $\tau_s = \rho_g s (\rho_g c_s)^{-1}$ (Weidenschilling 1977), which depends on particle size s and local sound speed c_s . The Epstein regime considers particles smaller than the mean free path of gas. Larger particles have to be treated in the Stokes regime. However, as long as relative velocities between dust and gas are small, it is possible to describe the coupling force as linear with respect to the relative velocity $f = m \frac{\delta u}{\tau_s}$, which is independent of the detailed calculation of τ_s . In particular, it is not necessary to determine the shape and density of the particles or the gas density and sound speed until one asks for the particle size corresponding to a given friction time.

This particle gas coupling is usually expressed in terms of the dimensionless Stokes number $\text{St} \equiv \Omega \tau_s$. Particles of different sizes, shapes, and densities, but ultimately with the same St, will behave the same as far as aerodynamics are concerned.

The friction time and thus the Stokes number is a function of the local gas density. Nevertheless, we assume that the Stokes number is constant, which is justified as the gas density fluctuates only by a few percent in the sub-sonic turbulence that we consider in our simulations.

Since our simulations are only 2D, we cannot consider the vertical settling of particles. The fact that the real 3D gas disk is vertically stratified and thus particles of a given size have a vertically varying friction time, must be discussed in more detail. One can interpret this approximation as focussing on a narrow vertical range around the midplane, in which neither the gas nor the particle stratification are too strong. Then, one can assume that also the friction time and the dust-to-gas ratio has no strong vertical variations. This assumption is a little less stringent than saying that all particles are actually in the midplane.

The general, the behavior of particle drift in a non-laminar yet geostrophic flow⁴ can be understood easily from a simplified treatment of the Lagrangian equations of motion for gas and dust:

$$\partial_t \mathbf{u} = \mathbf{F} - \frac{1}{\rho_g} \nabla p - \frac{\rho_d}{\rho_g \tau_s} (\mathbf{u} - \mathbf{v}) \quad (2)$$

$$\partial_t \mathbf{v} = \mathbf{F} - \frac{1}{\tau_s} (\mathbf{v} - \mathbf{u}), \quad (3)$$

where \mathbf{v} is the particle velocity and \mathbf{F} collects the terms that are the same for both dust and gas, e.g., gravitational force from the central star. The second term of these equations describes the pressure force, and the third term is the friction force between gas and dust particles. With some math, it can be shown that by subtracting Equations (2) and (3) and assuming $|\partial_t \mathbf{u} - \partial_t \mathbf{v}| \ll |\mathbf{u} - \mathbf{v}| / \tau_s$ particles will move toward regions with higher pressure $\mathbf{v} = \mathbf{u} + \tau_s \nabla p$ even if the pressure maximum is tiny and the profile is relatively smooth (see, e.g., Klahr & Lin 2001).

The vortices we consider are anti-cyclonic vortices and have a slightly lower epicyclic frequency than the Keplerian orbital frequency. Since there is a geostrophic balance between the

⁴ In a geostrophic flow, the pressure gradients are in equilibrium with the centrifugal and Coriolis acceleration.

Coriolis and the pressure force, a high pressure region inside the vortex is created. Particle accumulation inside a vortex then basically works the same way as the radial drift in an accretion disk. The particles do not feel the pressure gradient inside the vortex and, therefore, their epicyclic frequency equals the Keplerian frequency. However, the rotation frequency of a pressure supported vortex is smaller than the epicyclic frequency. Thus the headwind from the gas causes the particles to lose eccentricity and forces the particles to spiral toward the center of the vortex. For an in-depth analysis of vortex capturing, including a comparison of all forces acting on the gas and dust inside the vortex, see Adams & Watkins (1995), Barge & Sommeria (1995), Tanga et al. (1996), Chavanis (2000), and Johansen et al. (2004).

If the dust density becomes comparable to the gas density, the drag forces from particles onto the gas can no longer be neglected as long as the St is smaller than ≈ 10 . This back-reaction can alter the motion of the gas and also leads to even higher dust concentrations through the streaming instability (Youdin & Goodman 2005). The last term of Equation (2) represents the back-reaction from dust grains onto the gas.

3. NUMERICAL SETUP

We perform 2D shearing sheet simulations with the PENCIL CODE where we consider the vertically integrated densities Σ instead of the 3D densities ρ . The Euler-equations for the gas are solved on a Cartesian grid, identical to the setup of Raettig et al. (2013), but now augmented by a term for the particle feedback on the gas $\varepsilon(\mathbf{u} - \mathbf{v})/\tau_s$ with the dust-to-gas ratio $\varepsilon = \Sigma_d/\Sigma_g$

$$\frac{D\Sigma_g}{Dt} + (\mathbf{u} \cdot \nabla)\Sigma_g = -\Sigma_g \nabla \cdot \mathbf{u} + f_D(\Sigma_g), \quad (4)$$

$$\begin{aligned} \frac{D\mathbf{u}}{Dt} + (\mathbf{u} \cdot \nabla)\mathbf{u} = & -\frac{1}{\Sigma_g} \nabla p - 2\Omega_0(\hat{\mathbf{z}} \times \mathbf{u}) \\ & + \frac{3}{2}\Omega_0 u_x \hat{\mathbf{y}} + \frac{\beta p_0}{R_0} \left(\frac{1}{\Sigma_g} - \frac{1}{\Sigma_0} \right) \hat{\mathbf{x}} \\ & + f_\nu(\mathbf{u}, \Sigma) - \frac{\Sigma_d}{\Sigma_g \tau_s} (\mathbf{u} - \mathbf{v}), \end{aligned} \quad (5)$$

$$\begin{aligned} \frac{Ds}{Dt} + (\mathbf{u} \cdot \nabla)s = & \frac{1}{\Sigma_g T} \left\{ \nabla \cdot (K \nabla T) - \Sigma_g c_v \frac{(T - T_0)}{\tau_{\text{cool}}} \right. \\ & \left. + \frac{\beta p_0}{r_0} \frac{u_x}{(\gamma - 1)} \right\} + f_K(s). \end{aligned} \quad (6)$$

Here, Σ_g is the gas density, \mathbf{u} is the deviation of the gas velocity from the Keplerian value, s the entropy, T the temperature, c_v the specific heat at constant volume, τ_{cool} is the thermal relaxation timescale, and K the heat conductivity. The symbol

$$\frac{D}{Dt} \equiv \frac{\partial}{\partial t} + u_y^{(0)} \frac{\partial}{\partial y} \quad (7)$$

represents the Keplerian derivative, where $u_y^{(0)} = -3/2\Omega_0 x$ and Ω_0 is the Keplerian frequency at the orbit of the shearing box R_0 . The radial deviation from R_0 is given by x and the linearized azimuthal direction is now measured in terms of y . Boundary conditions are periodic in y and shear-periodic in x .

Further terms in the equations are diffusion terms to ensure numerical stability of the finite difference Pencil Code $f_D(\Sigma_g)$, $f_\nu(\mathbf{u}, \Sigma)$, $f_K(s)$ and radial stratification of the disk in terms of pressure and entropy for radially constant density: $\beta = -\frac{d \log p}{d \log R} = -\frac{d \log s}{d \log R}$. The stratification term β occurs in the linearized component of radial buoyancy (Equation (5)) and in the term for radial transport of entropy (Equation (6)) as derived in Lyra & Klahr (2011). These terms in combination with thermal relaxation are the drivers of vortices, as found in Petersen et al. (2007a). As described in their paper, gas that is moving radially outward is generally warmer and of lower density than gas moving inward. The density mismatch across the vortex leads to a mismatch in buoyancy and thus a vortex will feel a torque accelerating it. The maximal amplification occurs when thermal relaxation is on the same order as the internal rotation period of the vortex.

The dust grains are modeled with a particle approach. For each individual particle, we solve the equation of motion including gas drag. We do not allow for self-gravity thus far. In principle, for an individual particle it does not matter if there are other particles in the simulation or not. However, in the simulations where we allow for back-reaction of the particles on the gas, there is an indirect influence of one particle on the other particles due to the altered gas velocity.

The gas disk is co-rotating with Keplerian velocity at the co-rotational radius r_0 . However, for simulations involving both dust and gas, we need to include a velocity offset due to the pressure gradient. The pressure gradient is balanced by the Coriolis force, which is the linearized expression for the radial centrifugal acceleration in the local co-rotating system

$$2\Omega u_y = \frac{1}{\Sigma_g} \frac{\partial p}{\partial r} = c_s \Omega \frac{H}{r} \frac{\partial \ln p}{\partial \ln r}. \quad (8)$$

The deviation by which the gas velocity is lower than the Keplerian velocity $u_K = \Omega r$ is (Nakagawa et al. 1986)

$$\eta = 0.5 \left(\frac{H}{r} \right)^2 \frac{\partial \ln p}{\partial \ln r}, \quad (9)$$

which leads to a sub-Keplerian gas velocity and a deviation from the Keplerian velocity u_K of

$$u_y = 0.5 \left(\frac{H}{r} \right)^2 \frac{\partial \ln p}{\partial \ln r} \Omega r = \eta u_K. \quad (10)$$

This velocity deviation η is added to the simulations artificially.

For each particle i the equation of motion is solved individually via

$$\frac{d\mathbf{v}_*^{(i)}}{dt} = 2\Omega_{y_*}^{(i)} \hat{\mathbf{x}} - \frac{1}{2}\Omega_{x_*}^{(i)} \hat{\mathbf{y}} - \frac{1}{\tau_s} (\mathbf{v}_*^{(i)} - \mathbf{u}(\mathbf{x}^{(i)})), \quad (11)$$

where $\mathbf{v}_*^{(i)} = \mathbf{v} - \eta u_K$ is the particle velocity corrected by the velocity offset and $\mathbf{u}(\mathbf{x}^{(i)})$ is the gas velocity at the position of the dust particle. The index $*$ is omitted from now on.

For our 2D simulations, we choose $\eta = -0.01$, which corresponds to a pressure gradient of $\beta = 2.0$ and a disk aspect ratio of $h = 0.1$. The terminal velocities of the particles for a given Stokes number in a laminar disk are now in terms of η (Weidenschilling 1977)

$$v_x = \frac{2\eta u_K}{St + St^{-1}}, \quad (12)$$

$$v_y = \frac{\eta u_K}{St^2}. \quad (13)$$

These are the best assumptions one can make for the initial velocities of particles in our simulations.

Our physical domain spans four disk scale-heights, $\pm 2H$, around the co-rotational radius in radial-direction (x axis) and $16H$ in azimuthal-direction (y axis). The grid itself consists of 288^2 grid cells.⁵ We choose $\beta = 2.0$ for the entropy and pressure gradients. This is a relatively strong gradient compared to the gradients we expect in protoplanetary accretion disks, which are between $\beta = 0.5$ and $\beta = 1.0$. However, Raettig et al. (2013) found that the general behavior of vortices is the same for weak and strong entropy gradients. The development of the vortices is merely faster with stronger gradients and we can scan a large parameter space with a reasonable amount of computing time. For a first estimation, the strong gradient is sufficient, but in our future 3D studies including self-gravity we will use $\beta = 1.0$ because then we will be aiming for quantitative results on planetesimal formation rates and the mass spectrum.

We first evolve the disk for 200 local orbits without particles. This way, we make sure that a fully grown, long lived vortex has developed before we add particles. Physically, this corresponds to various scenarios: (A) a vortex developing in the outer parts of the disk and then migrating inwards through regions with particles, (B) the growth of particles into a size regime where they get trapped by the nearest vortex, or (C) a radial flux of particles close to bouncing and/or a drift barrier that enters the vicinity of the vortex.

After the initial 200 orbits, we distribute 400,000 particles randomly in the disk. This corresponds to four to five particles per grid cell initially. Therefore, we minimize numerical effects that can arise if there are not enough particles in the computational domain, e.g., the effect of a single particle can be extremely overestimated if not enough particles are considered. Whenever we refer to times in this paper, we mean the time elapsed since particles were added to the simulation. At the time when the dust-to-gas ratio approaches unity and streaming instability is triggered, 500 or more particles are in one grid cell. Following Johansen & Youdin (2007), these numbers are safely beyond the minimum particle number per grid cell needed to achieve numerical convergence.

Starting our simulations with particles included would not have changed our results very much as the initial and average dust-to-gas ratios are much too low for the dust to have an impact on the gas dynamics right from the beginning. Retrospectively, this assumption was later justified in simulations (see Section 4.2) in which the vortex is disrupted via the streaming instability and then forms again, this time in the presence of dust grains. This second growth phase does not differ from the initial growth phase without dust grains present.

Each of the 400,000 particles represents one super-particle, a collection of several particles, all of the same size, and a given mass according to the initial dust-to-gas ratio.

Generally, we have an initial dust-to-gas ratio ε_0 of 1:100, which means that the disk consists of 1% solid material and 99% gas. Note that in two dimensions the PENCIL CODE assumes surface densities instead of volume densities. Therefore, the

⁵ The number of 288 grid cells comes from the architecture of our computational cluster, which needs a multiple of 12 to parallelize the PENCIL CODE efficiently.

Table 1
Simulation Setup and ε_{\max}

Run	St	$\Sigma_{d,0}/\Sigma_{g,0}$	Feedback	ε_{\max}	Fraction of M_d with $\varepsilon \geq 0.01$ (%)	Fraction of M_d with $\varepsilon \geq 1.0$ (%)
NF 1	0.01	1:100	No	6.26	86.64	2.88
NF 2	0.05	1:100	No	636.00	92.31	75.63
NF 3	1.0	1:100	No	843.70	79.71	1.26
NF 4	20.0	1:100	No	46.81	99.90	99.80
F1	0.01	1:100	Yes	1.07	70.40	0.00
F2	0.05	1:100	Yes	3.86	95.24	2.13
F3	1.0	1:100	Yes	77.33	98.73	83.74
F4	20.0	1:100	Yes	0.73	79.82	8.09
DG 1	0.05	1:1000	Yes	1.15	86.74	0.00
DG 2	0.05	1:10,000	Yes	0.70	78.30	0.00
DG 3	1.0	1:1000	Yes	11.53	98.46	56.37
DG 4	1.0	1:10,000	Yes	4.17	97.30	76.15

dust-to-gas ratios we talk about in this paper refer to $\varepsilon = \Sigma_d/\Sigma_g$ rather than $\varepsilon = \rho_d/\rho_g$. To simulate different particle sizes, we use different Stokes numbers of $St = 0.01$, $St = 0.05$, $St = 1$, and $St = 20$. By only defining the Stokes Number, we are able to cover particles both in the Epstein as well as in the Stokes regime as friction forces are linear with respect to velocity. At 5 AU, this corresponds to particles between 3 mm and 6 μ m for $\Sigma_g = 300 \text{ g cm}^{-2}$ and $\rho_g = 2 \text{ g cm}^{-3}$. The parameters for all of our simulations can be seen in Table 1. A separate simulation is carried out for each St.

Particle growth due to collisions is not treated in our simulation. Physically, particles would have a growth time of several thousand years; therefore, we neglect this effect for the sake of keeping the simulation simple and easily evaluated.

4. RESULTS

4.1. No Particle Feedback

We first consider simulations where we do not include back-reaction from the particles, effectively setting $\rho_d = 0$ in Equation (5). That means that gas drags particles along, but even high dust densities do not affect the gas velocity in any way. The purpose of these simulations is to serve as comparisons to the later models in which feedback is included.

Figure 1 shows the maximum dust-to-gas ratio for these simulations. We see from the almost constant dashed-dotted green line that all of the available solid material in the $St = 1.0$ particle simulations accumulates in the vortex. This corresponds to a particle concentration for $St = 1.0$ particles of $c \approx \Sigma_d/\Sigma_{d,0} \approx 12,000$ and $\varepsilon \approx 320$. $St = 0.05$ particles eventually also accumulate within the vortex and then are kept trapped there. The maximum particle concentration is reached sooner for $St = 1$ particles than for $St = 0.05$ particles, which can be attributed to their higher radial drift velocity. Even for $St = 0.01$ particles, the dust-to-gas ratio increases to $\varepsilon \approx 1$.

We see two different behaviors. For $St = 0.05$ and $St = 1.0$, basically all of the particles are collected within the vortex, though $St = 0.05$ particles take 10 times longer. However, in both cases, concentrations of about four orders of magnitude are reached. For $St = 0.01$ concentration inside the vortex is only by two orders of magnitude and $St = 20.0$ particles concentrate by one order of magnitude, but, interestingly,

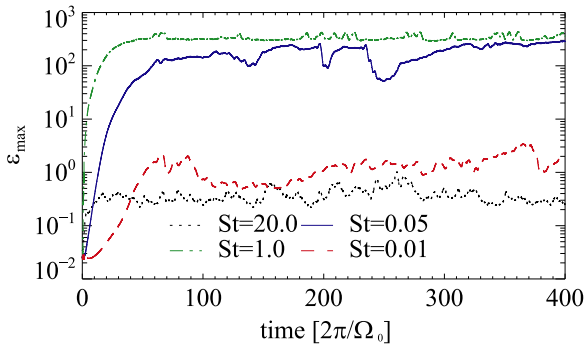


Figure 1. Maximum dust-to-gas ratio, ϵ_{\max} , for simulations without particle feedback. The different lines represent the different particle sizes: dotted (black) line: $St = 20$, dashed-dotted (green) line: $St = 1$, solid (blue) line: $St = 0.05$, and dashed (red) line: $St = 0.01$. Almost all particles of intermediate size ($St = 1.0$ and $St = 0.05$) accumulate in the vortex. Strongly coupled particles ($St = 0.01$) only partly accumulate inside the vortex, because they also couple to the gas outside of the vortex. Large particles ($St = 20$) hardly couple to the gas at all and, therefore, are not affected by the vortical gas motion.

outside the vortex in correlation with the zonal flow related to the radial position of the vortex (see Figure 2). These zonal flows show up in the azimuthally averaged rotation profile, both in magnetohydrodynamical simulations (Lyra et al. 2008b; Johansen et al. 2009; Dittrich et al. 2013) and in our hydrodynamical simulations of vortices. The zonal flows are deviations from the sub-Keplerian mean rotation profile confined by long-lived radial pressure variations (geostrophic balance).

The different behavior of particle accumulation can be explained through gas coupling. Particles with $St = 0.01$ are strongly coupled to the gas. As an effect, it takes much longer to capture the particles into the vortex and as a second effect the deviation between the actual vortex and an analytical solution, for instance a Kida vortex (see discussion in Lyra & Lin 2013), prevents the particles from accumulating too densely. An additional effect to prevent concentrations that are too strong in 3D vortices might be turbulence, triggered for instance by elliptical instability (Lyra & Lin 2013) and internal circulation (Meheut et al. 2012a). The $St = 20$ particles are the other extreme: they are hardly coupled to the gas at all, and, therefore, are only weakly affected by the vortical motion of the gas. In a stationary analytic vortex, these particles would get trapped if one waited long enough. However, our numerical vortex is dynamically active in changing its strength and shape and additionally drifting in the radial direction. This vortex dynamics gives the large particles a chance to escape from the vortex again, but they are still stopped by radial drift in the zonal flow.

4.2. Including Particle Feedback

In the last Section, we showed that there are significant particle overdensities within the vortex. This means that we cannot neglect the momentum transfer from dust onto gas. Because of this, we now include a dust back-reaction on the gas, using the full Equation (5).

For the $St = 20.0$ particles, there is no change with respect to the simulations without particle feedback because overdensities stay below $\epsilon = 1.0$ (compare the left and right sides of the top panel in Figure 3). For these large particles, the streaming instability cannot be triggered at the present dust-to-gas ratio.

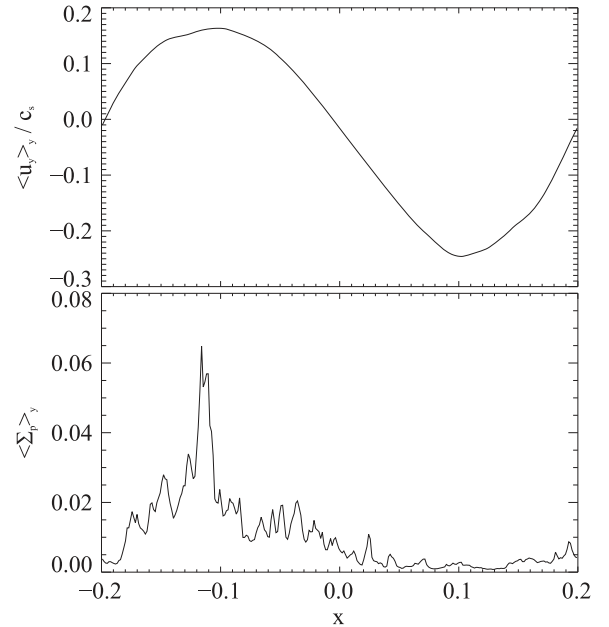


Figure 2. Azimuthally averaged gas velocity and particle density for $St = 20.0$ particles. The particles accumulate in the zonal flow structure.

All other tested particles still accumulate in the vortex, yet differently, as follows.

Particles with $St = 1.0$ concentrate more locally (in a smaller area) than smaller particles (bottom panel of Figures 3 and 4). $St = 1.0$ particles are getting concentrated on timescales that are not longer than the dynamical timescale of the vortex (Barge & Sommeria 1995), thus they can easily follow the changes of the vortex in shape, strength, and location. Smaller particles have much longer timescales to spiral into the center of the vortex—longer than the dynamical timescale of the vortex. As the attractor inside the vortex is changing its location on dynamical timescales (change of amplitude, shape, and location of the vortex), the particles have no chance to ever catch up or follow it.

An effect that occurs when ϵ approaches unity is the streaming instability (Youdin & Goodman 2005; Youdin & Johansen 2007). Once particles concentrate, their locally increased dust-to-gas ratio leads to a slower radial drift (Nakagawa et al. 1986). This produces a further enhancement of solids since faster particles from slightly larger radii bump into the accumulation, like a traffic jam, which eventually results in streaming dust structures. This is also the case in our simulations, though with our resolution it is possible to resolve only part of the unstable wavelengths. Therefore, we are not able to study the linear and nonlinear behavior of the streaming instability in full detail or model the correct growth rates of the instability. However, for the wavelength, we find the correct threshold dust-to-gas ratio to trigger the instability. Also see the Appendix for additional resolution tests on the streaming instability.

Figure 5 shows the vertical gas vorticity ω_z in units of the local Keplerian frequency Ω_0 and dust-to-gas ratio $\epsilon = \Sigma_g / \Sigma_d$ for a simulation with $St = 0.01$ particles after 300 local orbits (run F1). It is clear that the particles accumulate inside of the vortex and follow the vortical motion. Where the concentration is highest, they create strong maxima in the gas vorticity. This is an effect of the cyclonic rotation of the particle clumps,

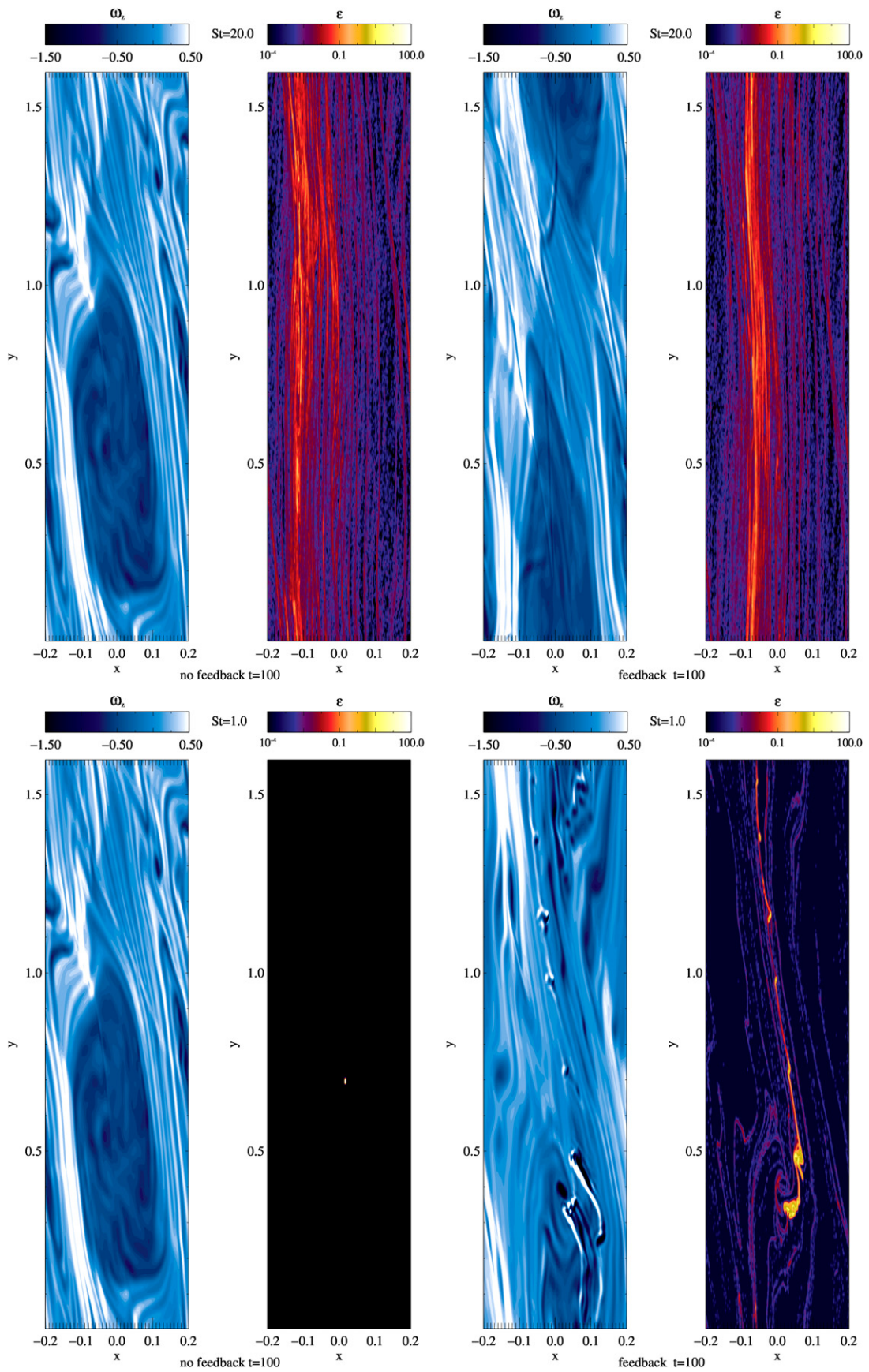


Figure 3. Vorticity ω_z in units of the local Keplerian frequency Ω_0 and the dust-to-gas ratio without particle feedback (left), including the back-reaction (right) for $St = 20.0$ (top) and $St = 1.0$ (bottom) particles.

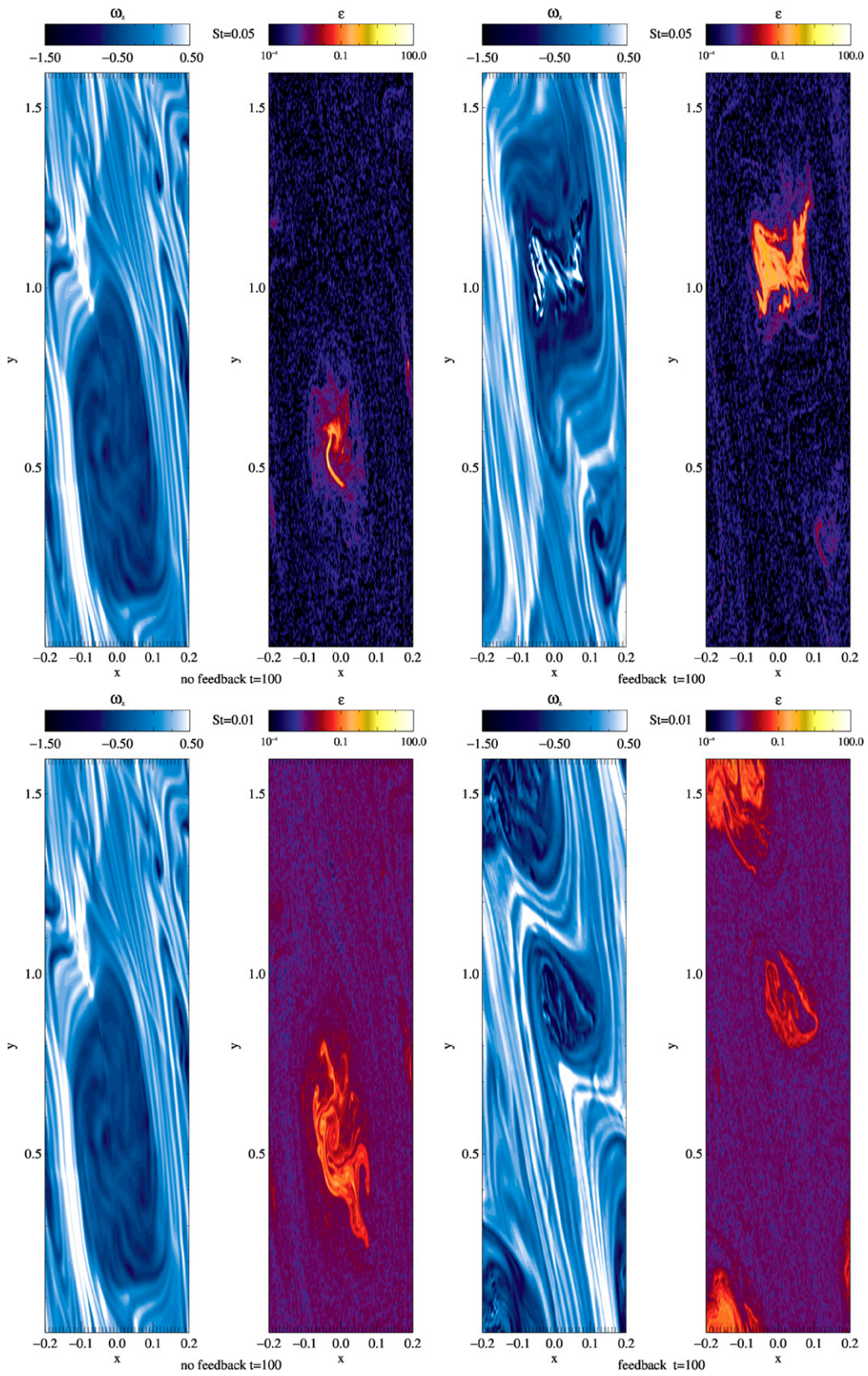


Figure 4. Vorticity ω_z in units of the local Keplerian frequency Ω_0 and dust-to-gas ratio without particle feedback (left), including the back-reaction (right) for $St = 0.05$ (top) and $St = 0.01$ (bottom) particles.

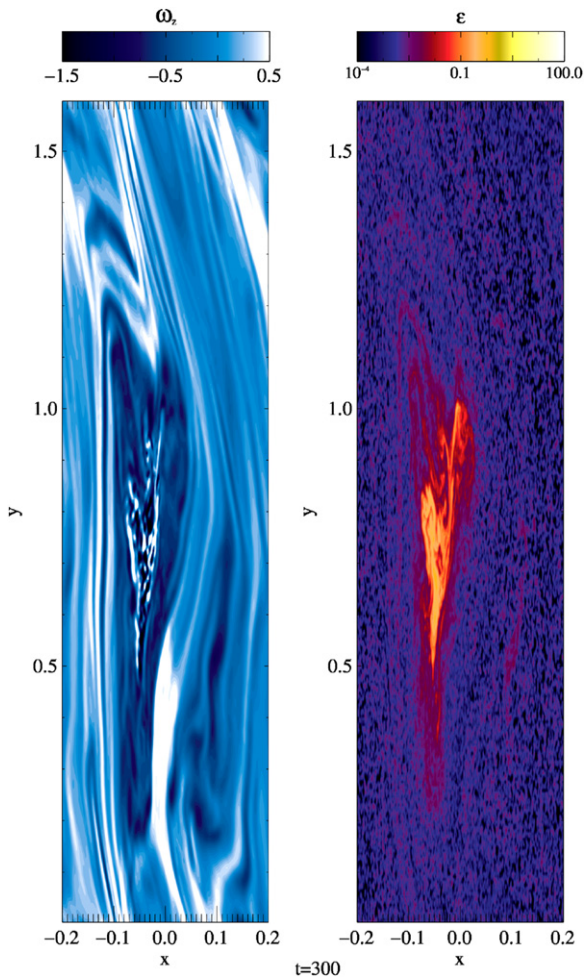


Figure 5. Vorticity of the gas flow (left panel) and dust-to-gas ratio (right panel) for a simulation with $St = 0.01$ particles and back-reaction onto the gas. The elliptical vortical gas flow is distinguishable in the vorticity plot. There are strong accumulations of particles within the vortex. Although many particles spread out over the entire vortex, most particles concentrate in the center of the vortex. The positive vorticity values in the vortex (light areas in the left plot) show the effect that particles have on the gas. Where the gas encounters obstacles, namely high particle concentrations, steep vorticity gradients develop.

which was already reported in Lambrechts & Johansen (2012) and is a consequence of the conservation of angular momentum under contraction, which can turn anticyclonic motion in a rotating system to cyclonic motion.

In general, due to the back-reaction of the dust on the gas and the resulting streaming instability, the initially elliptical gas streamlines are bent into more complex motions than in cases without a back-reaction.

In the case of $St = 1.0$ particles, where the local particle concentration and, therefore, the back-reaction are strongest, the vortex structure is disrupted. Because of this, the particle trapping mechanisms lose strength: pressure gradients across the vortex become shallower, Coriolis forces in the vortex grow weaker, and the particles begin to escape the vortex. Because the local particle concentration decreases, the large vorticity gradients flatten out again. This eventually leads to a new amplification of the vortex due to the background stratification and the process repeats itself (see the series of snapshots in Figure 6).

The destruction of the vortex occurs on very short timescales set by the streaming instability, whose growth time is a function of the dust-to-gas ratio and Stokes number of the dust that can be as fast as one orbital period (Johansen & Youdin 2007). The new vortex amplification on the other hand takes hundreds of orbits, such as in the initial growth, because it depends on the radial stratification of the disk and the thermal relaxation time of gas.

This vortex disruption and reforming process discussed here is not to be confused with the vortex instability discussed in Chang & Oishi (2010). They analyze the stability of a 3D vortex based on the density contrast between the interior of a vortex and the ambient medium and determine that if this contrast is higher than a few 10% then the vortex will become unstable. Although we see such high dust density concentrations inside the vortex, they are very localized and, therefore, our vortices remain stable. For them to become entirely unstable, according to Chang and Oishi’s analysis, the density contrast needs to be uniformly high and spread out over the entire vortex, which is never the case in our simulations.

Figure 7 shows the maximum dust-to-gas ratio of our different simulations with different St . We clearly see that $St = 1.0$ particles (dashed-dotted green line) have the highest concentrations. As the particle size decreases, the concentration also decreases. It is important to note that $St = 20.0$ particles do not accumulate inside the vortex. The highest dust-to-gas ratio is reached for $St = 1.0$ particles. Larger and lower St reach lower dust-to-gas ratios.

We now turn our attention to the spatial distribution of the dust concentration. By clustering, we understand what fraction of the dust takes part in the high overdensities, which are the particles triggering the streaming instability. In Figure 8, we show what fraction of the entire dust content M_d has a specific dust-to-gas ratio. The dashed vertical lines indicate the initial dust-to-gas ratio $\epsilon_0 = 0.01$ and $\epsilon = 1.0$. For $St = 1.0$ particles, 83.74% have accumulated in regions with $\epsilon \geq 1.0$, whereas, for $St = 0.05$, particles only 2.13% of the entire dust mass is concentrated in areas with $\epsilon \geq 1.0$. The remaining dust is spread out thinner. All results can be seen in the seventh and eighth columns of Table 1. Note that for the clustering we considered a temporal average, but for the maximum dust-to-gas ratio ϵ_{\max} (fifth column in Table 1) we took the absolute maximum from the entire run. Therefore, for runs F1 and DG 1 $\epsilon_{\max} > 1.0$ at a given moment while on a temporal average this value is not reached. A dust-to-gas ratio of $\epsilon = 1.0$ is significant, because that is when the dust back-reaction on the gas becomes important. This means that for $St = 1.0$ the back-reaction is a requirement if we want to realistically model particle behavior. However, for larger St , it seems that the back-reaction, including the streaming instability, contributes little to the overall dynamical behavior of particles. However, we already saw that there is a significant difference between the simulations with and without particle feedback for $St = 0.05$ particles (see Figures 1 and 7). Without feedback, all particles were accumulated in the vortex whereas the maximum dust-to-gas ratio with feedback was around two to eight, two orders of magnitude lower. This is confirmed by the Figure 9, where we compare the clustering of $St = 0.05$ particles with (dashed line) and without feedback (solid line). The particle accumulation is similar for low dust-to-gas ratios. However, as ϵ increases, streaming sets in for the simulation with feedback and thus regulates the overdensities. Without feedback, the overdensities

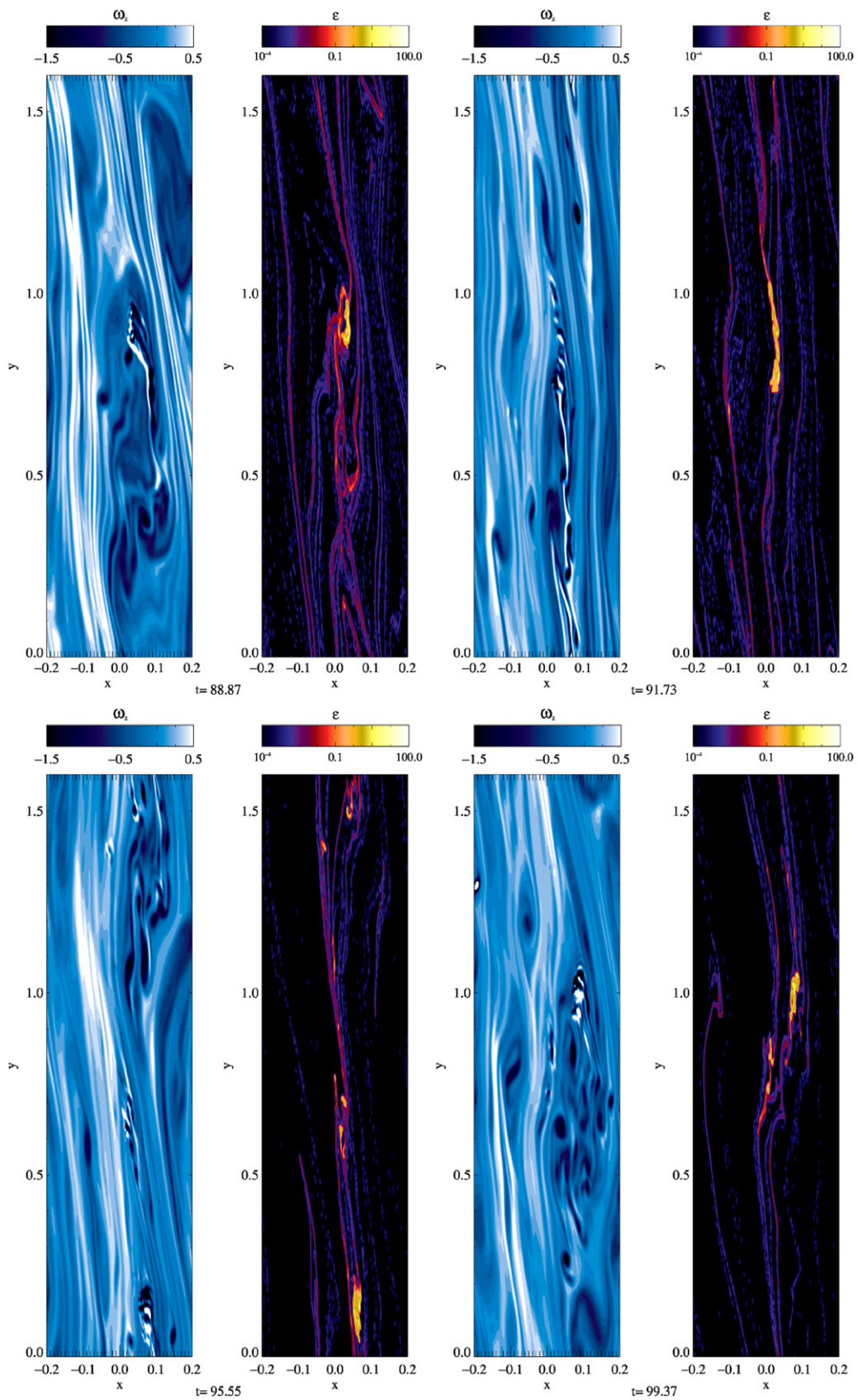


Figure 6. Vorticity ω_z in units of the local Keplerian frequency Ω_0 (first and third column) and dust-to-gas ratio (second and fourth column) for $St = 1.0$ particles for different points in time. At the first snapshot, the vortex is still clearly distinguishable. In the second snapshot, it has been strongly disrupted by the particle accumulation. As this particle accumulation spreads out, the vortex can slowly regain its shape (third snapshot) and form a large, yet still perturbed, vortex again (fourth snapshot).

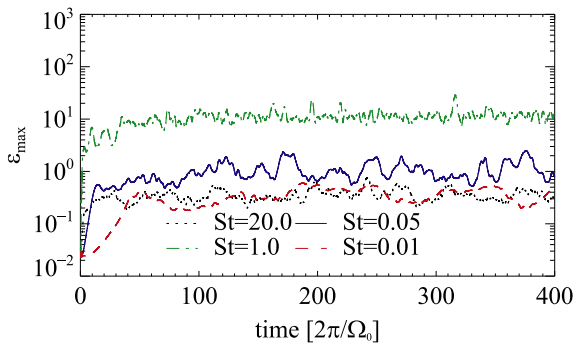


Figure 7. Maximum dust-to-gas ratio, ϵ_{\max} , for simulations with particle feedback. The different lines represent the different particle sizes: dotted (black) line: $St = 20$, dashed-dotted (green) line: $St = 1$, solid (blue) line: $St = 0.05$, and dashed (red) line: $St = 0.01$. Particles of $St = 1.0$ reach the highest dust enhancements and concentrate in a very local area in the vortex, while smaller particles spread out over the entire vortex. Therefore, the overdensities reached are lower.

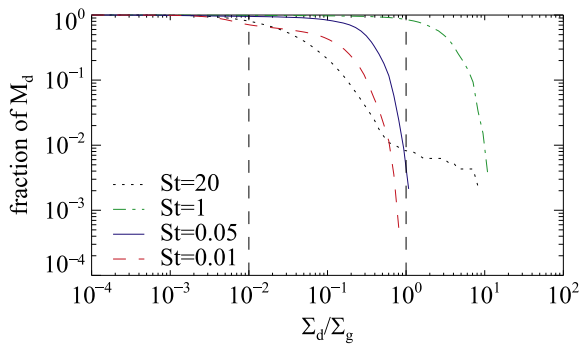


Figure 8. Fraction of the entire dust mass in a specific dust-to-gas ratio or higher. $\epsilon \geq 1.0$ are reached for all particle sizes. For $St = 1.0$ particles more than 80% of all particles have concentrated in areas with larger ϵ than 1.0.

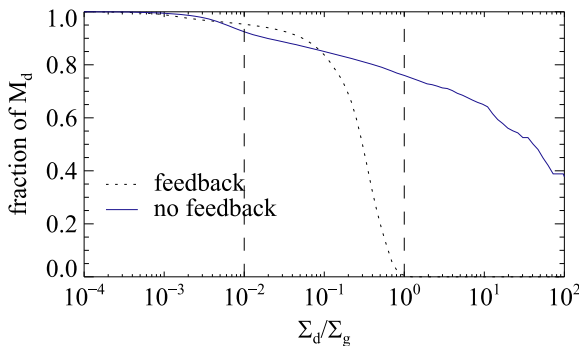


Figure 9. Fraction of the entire dust mass in a specific dust-to-gas ratio or higher. $\epsilon \geq 1.0$ are reached for $St = 0.05$ particles with (dashed black line) and without feedback (solid blue line).

can grow unhindered, which results in about 80% of all particles accumulating in $\epsilon > 1.0$. We want to stress that although the dust-to-gas ratios are different depending on whether the back-reaction is included or not, it might be difficult to distinguish such extremely large locally confined concentrations observationally with, e.g., ALMA (Lyra & Lin 2013). Also, for $St = 0.01$ particles that only reach $\epsilon_{\max} \approx 1.0$, we already saw that there is an effect on the gas (see Figure 5). In this context, one has to stress that growth rates and unstable wavelengths toward the streaming instability depend on the St as well as on the actual dust-to-gas ratio. A detailed study of the nonlinear evolution of the streaming instability and the

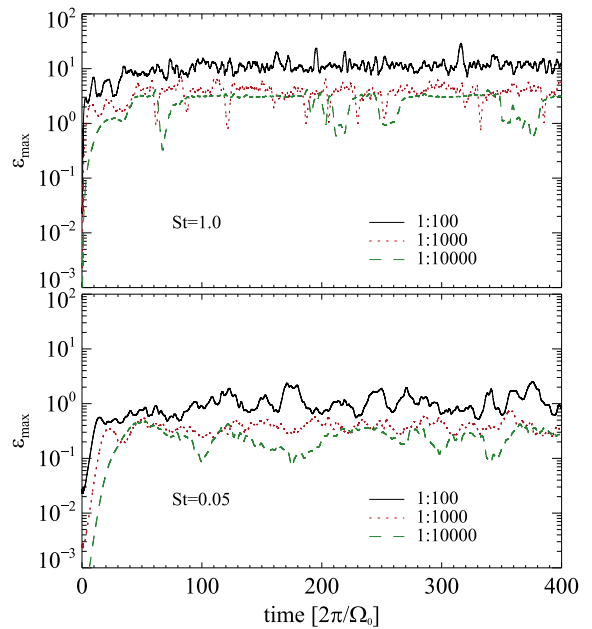


Figure 10. Particle concentration (solid lines) and maximum dust-to-gas ratios for $St = 0.05$ (top) and $St = 1.0$ (bottom) particles. The colors represent the different initial dust-to-gas ratios: 1:100 (black), 1:1000 (red), and 1:10,000 (green). More individual super-particles are captured in the vortices for a low initial ϵ , because their back-reactions are less efficient. Since each of these super-particles is less massive than with higher ϵ , the overall dust-to-gas ratio for low initial ϵ is lower than that of larger initial ϵ .

clumping caused by the streaming instability can be found in Johansen et al. (2009), who can afford a resolution that is 10 times higher than ours. One can interpret the simulations of Johansen et al. (2009) as a detailed study on the dust behavior inside a vortex concentration and, therefore, our vortices generate the dust-to-gas overdensities needed for the Johansen et al. (2009) scenario.

We conclude that as soon as even a fraction of particles approaches, a $\epsilon \approx 1.0$ back-reaction from the particles onto the gas needs to be included to accurately model their behavior.

4.3. Lower Dust-to-gas Ratios

Thus far, the considered initial dust-to-gas ratio was always $\epsilon_0 = 1:100$, but it has been shown that planets can also form in low metallicity disks (Niedzielski et al. 2009; Mordasini et al. 2012). It is also possible that planetesimal formation is still ongoing in a disk where some planets have already formed, such as in the 51 Peg system (Dumusque et al. 2012) and, therefore, the disk can be depleted in solids. A third reason to consider lower initial dust-to-gas ratios is the possibility that only a small fraction of the entire dust content is in the particle size regime that we study as a result of the coagulation-fragmentation balance, which was studied by Birnstiel et al. (2012). To account for this, we perform simulations with lower initial dust-to-gas ratios, such as $\epsilon_0 = 1:1000$ and $\epsilon_0 = 1:10,000$. The number of super-particles we add to the domain stays the same, while each super-particle represents less mass than in cases with higher initial dust-to-gas ratios.

Figure 10 shows the particle accumulation and resulting dust-to-gas ratios for $St = 0.05$ (simulations F2, DG 1, DG 2) and $St = 1$ (simulations F3, DG 3, DG 4). In cases with low ϵ_0 , more super-particles concentrate in one location. Since each of these super-particles has less mass compared to simulations

Table 2
Collisional Velocities

St	ϵ_0	α	v_{coll} [c_s]	$\frac{u_{\text{rms}}}{\sqrt{\alpha} c_s}$	$\frac{v_{\text{rms}}}{\sqrt{\alpha} c_s}$	$\frac{v_{\text{coll}}}{\sqrt{\alpha} c_s}$	$\frac{\Delta v_{\text{coll}}}{\sqrt{\alpha} c_s}$	$\frac{v_{\text{coll, OC}}}{\sqrt{\alpha} c_s}$
1.0	1×10^{-2}	1.03×10^{-2}	2.77×10^{-3}	2.84	1.37	2.73×10^{-2}	2.56×10^{-2}	1.0
1.0	1×10^{-3}	1.56×10^{-2}	3.17×10^{-3}	4.36	3.61	2.54×10^{-2}	3.34×10^{-2}	1.0
1.0	1×10^{-4}	1.54×10^{-2}	1.25×10^{-3}	3.88	2.27	1.01×10^{-2}	4.01×10^{-2}	1.0
0.05	1×10^{-2}	1.56×10^{-2}	2.86×10^{-3}	3.27	2.41	2.29×10^{-2}	5.87×10^{-3}	0.31
0.05	1×10^{-3}	1.57×10^{-2}	2.71×10^{-3}	4.29	3.80	2.16×10^{-2}	1.28×10^{-2}	0.31
0.05	1×10^{-4}	1.54×10^{-2}	2.08×10^{-3}	3.88	3.04	1.68×10^{-2}	9.40×10^{-4}	0.31

with higher dust-to-gas ratios, the back-reaction is less effective. Thus the absolute dust-to-gas ratio values to be reached in low metallicity systems are almost as high as in high metallicity systems. The gas is not affected as much by the dust particles as in previous simulations. Thus the vortices, though still disrupted slightly by the back-reaction, are no longer torn apart. The particles are trapped more tightly and cannot leave the vortex.

We conclude that the relative concentration in low metallicity disks is much stronger than in high metallicity systems, thus the absolute dust-to-gas ratio values to be reached in low metallicity systems is almost as high as in high metallicity systems. In the end, a roughly identical dust-to-gas ratio is always reached (within one order of magnitude $\hat{\text{e}}\text{d}g$), e.g., at the physical condition for triggering the streaming instability.

5. COLLISIONAL VELOCITIES

In our simulations, collisions between the particles are neglected. For the physical conditions of a protoplanetary disk with real particle numbers of a typical collision time, e.g., the time after all particles have collided once, is typically a few thousand orbits. With our super-particle approach, we have no chance to ever observe a real collision in the course of our simulation. Nevertheless, it is important to know collision speeds in order to study possible growth or disruption in statistical codes (e.g., Birnstiel et al. 2012).

Thus when we talk about collisional velocities, we mean relative velocities of neighboring particles from which we extrapolate likely collision speeds. In the following, we will discuss how we calculate their collisional velocities.

Since we use a 2D approach, our model can only provide first estimates for collisional velocities. For instance, we neglect small-scale turbulence that will arise from the vertical structure of the disk and particle layer (e.g., Kelvin-Helmholz: see Johansen et al. 2006a) and elliptic instability due to 3D waves propagating inside the vortex, but also from the tail of the Kolmogorov cascade that is not present in 2D simulations. In general, 2D flows tend to create large vortical structures rather than allowing energy to cascade down to the dissipation scale.

Therefore, we take a rather simple approach to estimate collisional velocities, which are basically the local dispersion in the particle velocities. More precisely, we consider each grid cell separately, since only particles that are close together have a chance to collide. From each individual particle's velocity v_i in a given grid cell, the mean particle velocity of all particles within this grid cell \bar{v} is subtracted. Afterwards, the average of these residual velocities within one grid cell is taken. This results in the mean collisional velocity within this grid cell. To get the average collisional velocity of the entire system v_{coll} , we

average over all grid cells that include at least 10 particles. The results can be seen in Table 2 for $\text{St} = 1.0$ and $\text{St} = 0.05$ particles. Figures 11 and 12 show the spacial distribution of the collisional velocities. Higher collisional velocities coincide with regions of high particle density.

For tightly coupled particles (low Stokes numbers) it is necessary to first subtract the local gas velocity at the position of a particle from v_i . Otherwise, we would measure the velocity dispersion of the gas rather than of the particles. This results in low collisional velocities Δv_{coll} , for the smaller $\text{St} = 0.05$ particles. This is not so much the case for $\text{St} = 1.0$ particles as they only marginally couple to the gas.

If we compare these collisional velocities to the theoretically predicted collisional velocities by Ormel & Cuzzi (2007), for a given turbulent α value, we see grave deviations. Already, our gas velocity u_{rms} , which is three to four times as large as the turbulent gas velocity $u_t = \sqrt{\alpha} c_s$, where α is a dimensionless viscosity parameter, Shakura & Sunyaev (1973) suggest a deviation from their model. For $\text{St} = 1.0$ particles, they predict a ratio of particle collisional velocities to turbulent velocities of 1.0, yet our value is of the order of 10^{-3} . This shows that the theory of Kolmogorov turbulence is not applicable to the vortex environment, at least as long as we neglect the third dimension and thus cannot predict particle collisions inside vortices accurately.

From our model, we see that the α values measured outside the vortex are not a good proxy to estimate the collisional velocities inside the vortex. In our 2D simulations, the vortex may appear calmer than it would actually be in 3D where elliptical instability can produce turbulence inside the vortex core (Lesur & Papaloizou 2010; Lyra & Klahr 2011).

However, as we stated before, this is a rather simple approach and these collisional velocities can only be seen as a first estimate. There are several factors that can increase the velocities. Higher resolution and a treatment of three dimensions will lead to properly resolving the streaming instability and with this particle velocities will increase (Johansen et al. 2009). Including the vertical stratification will increase particle velocities, too, as also the vortex dynamics become more complex.

It is not possible to quantify the error introduced by our 2D approximation. For that purpose, we have to wait until we have evaluated full 3D models, which are numerically wise significantly more expensive.

6. PARTICLES COLLECTED INSIDE THE VORTEX AND POSSIBLE GRAVITATIONAL COLLAPSE

Our 2D simulations tell us that the dust-to-gas ratio is significantly increased inside a vortex. A detailed study on gravitational fragmentation of the particle layer would require

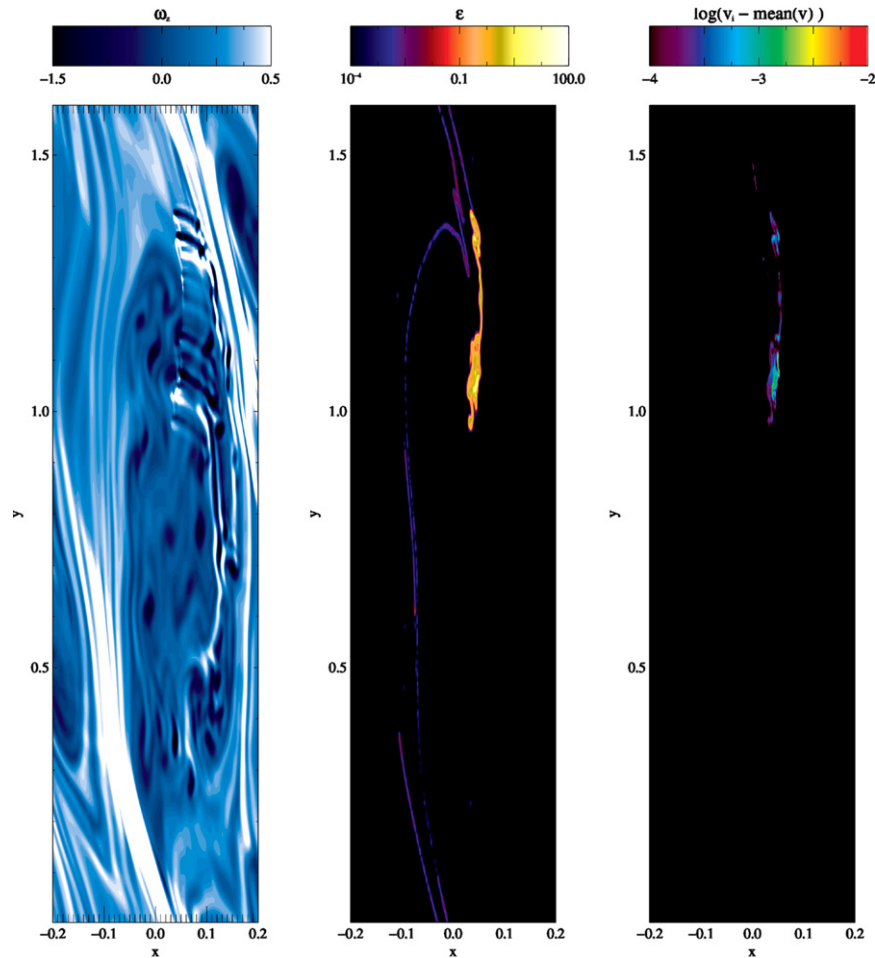


Figure 11. Vorticity ω_z in units of the local Keplerian frequency Ω_0 of the gas flow (left), dust-to-gas ratio (middle) and particle collisional velocity (right) for $St = 1.0$ particles, $\varepsilon_0 = 10^{-2}$ and after 200 local orbits. Collisional velocities are higher where high particle concentrations are located, but hardly exceed $10^{-3}c_s$.

3D modeling as the criterion for collapse to reach a critical 3D density of ρ_R , which is the Roche density. The Roche density is defined as the density of a clump that cannot be sheared apart by tidal forces from the central object.

It can be derived by equating the the gravitational acceleration on the surface of a clump

$$a_{g,c} = \frac{GM_c}{R_c^2}, \quad (14)$$

where M_c and R_c are the clump's mass and radius, respectively, with the tidal acceleration a_t on the clump's surface. The tidal acceleration is the difference between the gravitational pull of the central star at the clump's surface and its center of mass. To first order, we get

$$a_t \approx \mp 2R_c \frac{GM_\star}{r^3}, \quad (15)$$

where M_\star is the mass of the central object and r is the distance between the star and particle clump. If we now equate these two accelerations, exchange the masses by their respective densities, and solve for the clump density, we get

$$\rho_{\text{crit}} > \rho_R = \frac{3 M_\star}{2 \pi r^3}. \quad (16)$$

If the density of the particle clump is higher than this critical

density, it will be held together by its own gravity. If this is not the case, then the particle clump will be torn apart by tidal forces.

There are additional forces that act to prevent collapse besides gravitational tides, e.g., erosion and tides exerted by the vortex (Lyra et al. 2009b), but we only aim for a first estimate here and, therefore, neglect these forces.

If we take the mass of the Sun for the mass of the central object then we get $\rho_R(1 \text{ AU}) = 2.83 \times 10^{-7} \text{ g cm}^{-3}$ and $\rho_R(5.2 \text{ AU}) = 2.01 \times 10^{-9} \text{ g cm}^{-3}$. The highest overdensities we observed reached for $St = 1.0$ particles is $\Sigma_d \approx 80\Sigma_g$. This means that the trapping alone will in most cases not lead to Roche densities, yet we have neglected sedimentation. As was shown in Johansen et al. (2009), an increase in the metallicity of the disk by a factor of a few is sufficient to trigger both streaming instability and, in succession, gravitational collapse into planetesimals.

For $St = 0.01$ particles, for example, it is apparent from Figure 5 that the material inside the vortex structure reaches dust-to-gas ratios of $\varepsilon \approx 0.1$. This is a concentration in local available dust by a factor of 10. As shown by Johansen et al. (2009), a concentration by a factor of three would be sufficient to trigger planetesimal formation.

Nowhere outside the vortex are these ε values reached. Comparing this to the clustering in Figure 8, we see that about 40% of the entire particle fraction is in concentrations of

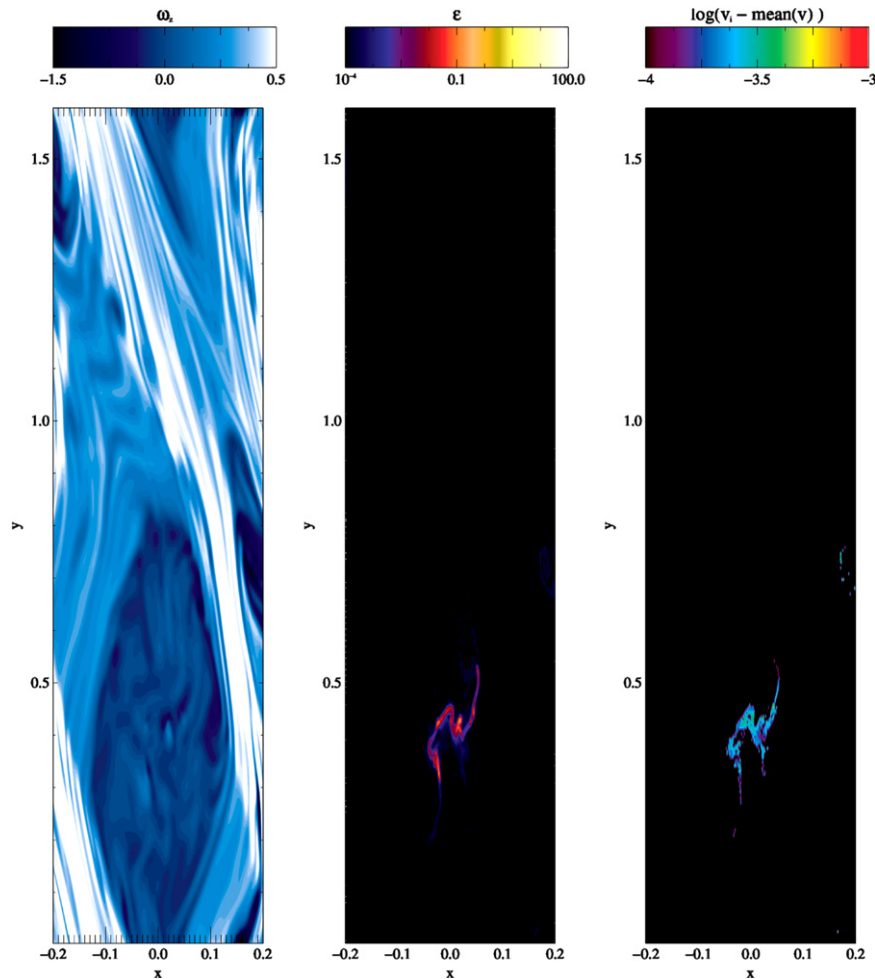


Figure 12. Vorticity ω_z in units of the local Keplerian frequency Ω_0 of the gas flow (left), dust-to-gas-ratio (middle) and particle collisional velocity (right) for $St = 0.05$ particles, $\varepsilon_0 = 10^{-4}$ and after 200 local orbits. Collisional velocities are higher where high particle concentrations are located, but hardly exceed $10^{-4}c_s$.

$\varepsilon \geq 0.1$ and thus about 40% of the entire particle fraction is captured inside the vortex. Doing the same analysis for the other particle sizes even leads to values of up to 98%, which means that the capturing mechanism is very efficient. Note that these are best case values, since in our simulation no material is lost. If a particle is not captured by the vortex the first time it passes it, it can be captured the second time due to the periodic boundaries, whereas, in a real disk, this particle would be lost to the vortex. On the other hand, we also neglect the influx of particles from larger radii (see Birnstiel et al. 2012), thus one can argue that our fixed global metallicity is a conservative underestimation, as even more material might end up in the vortical trapping region.

7. SUMMARY AND CONCLUSION

In this paper, we analyze how particles and vortices sustained by the radial stratification of a disk affect each other. In particular, we investigated whether particles of various sizes can be trapped inside and thus concentrate in vortices and whether the vortices remain a long lived phenomenon if feedback of particles onto the gas is considered.

We have conducted two sets of simulations for a set of Stokes numbers ($St = 20.0$, $St = 1.0$, $St = 0.05$, and $St = 0.01$): one where there is only gas drag on the particles and one where particles also exert drag on gas. This becomes

important if the initial dust-to-gas ratio is locally enhanced from 0.01 to about 1.0.

We see that without a back-reaction, $St = 0.05$ and $St = 1.0$ particles are swept up very efficiently by the vortices and, in the case of the $St = 1.0$ particles, they even concentrate all in one single grid cell. Whereas smaller and larger particles can escape from the vortex again because smaller particles are too slow to follow the dynamical evolution of the vortices in position, larger particles leave the vortex in the azimuthal direction, yet they get trapped in the zonal flow correlated with the radial position of the vortex.

If we include particle feedback, then we get a more complicated picture. $St = 20.0$ particles are hardly affected by the vortex structure and no critical particle concentration to trigger the streaming instability is reached. Therefore, the gas and the vortex are not affected by the large particles. In conclusion, $St = 20$ particles are neither captured inside the vortex nor would they stay inside the vortex if they would be coagulations products from inside smaller material, e.g., $St = 0.01$ – 0.05 . However, we want to stress that we again see particles getting trapped in the zonal flow related to the vortex, an effect that has already been checked in global simulations (Figure 11 in Lyra et al. 2009b).

For all smaller particles, we see a high concentration of particles inside the vortex. $St = 1.0$ particles concentrate very

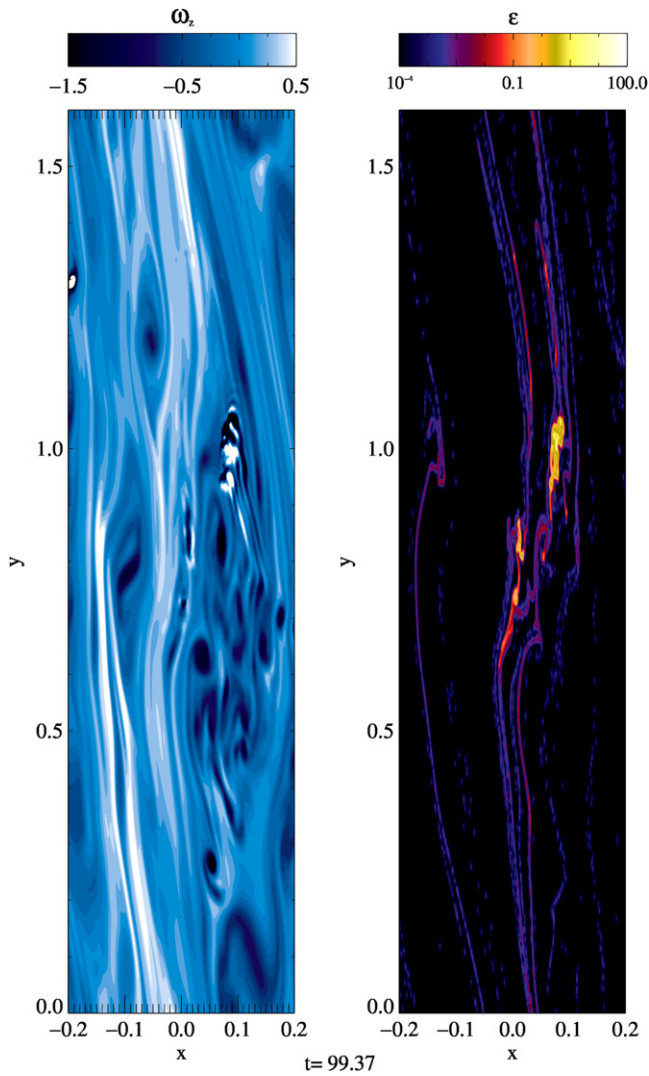


Figure 13. Gas vorticity ω_z in units of the local Keplerian frequency Ω_0 and dust-to-gas ratio for $St = 1.0$ particles with twice the standard resolution. Streaming is still clearly visible and there is no significant difference with respect to the lower resolution simulation (see Figure 3).

locally in the center of the vortex, which leads to streaming instability that appears as a strong vorticity perturbation that will eventually disrupt the vortex. With decreasing particle density, the vortex can be re-established and the cycle repeats. The dust-to-gas ratio can be locally increased up to $\varepsilon \approx 80$. More than 80% of the dust is concentrated to more than $\varepsilon = 1.0$.

Smaller particles are not so strongly concentrated inside the vortex. Instead, they are spread out over the entire vortex and take part in the streaming instability (Youdin & Goodman 2005; Youdin & Johansen 2007). This instability typically shows up when $\varepsilon > 1.0$ even when only a small fraction of the available dust takes part in the instability. For $St = 0.05$ particles, only 2.13% of the entire mass reached $\varepsilon > 1.0$. The maximum dust-to-gas ratios reached are $\varepsilon \approx 3.0$ for $St = 0.05$ and $\varepsilon \approx 1.0$ for $St = 0.01$.

Although the particle concentrations achieved are quite different for the different particle sizes, the overall mass of particles accumulated in a vortex is roughly the same, which matches the analytical prediction of Lyra & Lin (2013) quite

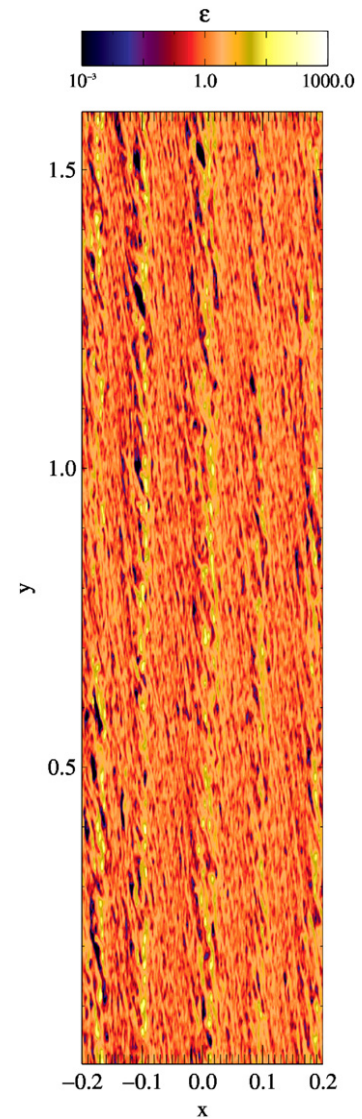


Figure 14. Dust-to-gas ratio for $St = 1.0$ particles, an initial dust-to-gas ratio of $\varepsilon_0 = 3.0$ and no vortex. Clumping of particles still happens; therefore, the streaming instability is not an effect of the vortex capturing alone. It can also be resolved with standard resolution and without radial stratification.

well. Around 90% of the entire dust content is swept up by the vortex, which corresponds to a dust density that is about four times higher inside the vortex than in the background without having a vortex and about 30 times higher than in the region outside the vortex. This nicely highlights the prospects of detecting vortices by their enhanced dust-to-gas ratio (Wolf & Klahr 2002; van der Marel et al. 2013).

We also conducted simulations with lower initial dust-to-gas ratios for three reasons: (1) to see whether planetesimal formation can be triggered around low metallicity stars, (2) to see if evolved dust populations in disks (with significant dust masses in at least planetesimal mass objects or already lost due to drag toward smaller radii) can still form planetesimals, and (3) to mimic a situation in which only a small fraction of the total dust content grows to a size of $St = 0.01 - St = 1.0$ as a result of the coagulation-bouncing-fragmentation-drift balance (Birnstiel et al. 2012). We see that although the initial dust-to-gas ratio ε_0 is a factor 10 or 100 lower, the locally reached maximal dust-to-gas ratio is still of the same order of

magnitude. The relative particle concentration increases until the back-reaction becomes significant, which is independent of the initial dust-to-gas ratio.

The first estimates of the collisional velocities of the dust particles are much lower than what is to be expected based on Kolmogorov turbulence of equivalent global α . These low velocities are possibly a result of our 2D approximation and will have to be tested in 3D simulations to accurately calculate collision speeds and its effect of limiting particle accumulation.

We confirm that baroclinic vortices are important mechanisms for accumulating particles even when feedback via drag is considered. The concentrations achieved are, depending on particle size, a factor of 100 to 10,000 higher than the average value. Even if there is only a low amount of dust present, these high overdensities can be reached. Streaming instability additionally enhances the dust concentration. Our 2D studies neglect the vertical structure of the gas disk and the dust layer. On the other hand, 3D studies are much more computationally expensive and would not have allowed us to scan the parameter range encompassed in this study.

The expected difference in 3D versus 2D simulations lies in the additional concentration effect by vertical sedimentation that is obviously not possible in 2D vertically integrated models. Additionally, the vortex itself is weaker due to the elliptic instability (Lesur & Papaloizou 2009; Lyra & Klahr 2011) and diffusion inside the vortex. Thus the 2D studies are a conservative underestimation of the maximal particle concentrations to be reached in full 3D, if we consider 3D vortices of the same strength as 2D vortices.

For a few selected physical parameters, we will study the interaction of vortices and dust in three dimensions next.

The authors gratefully acknowledge the Gauss Centre for Supercomputing (GCS) for providing computing time for a GCS Large Scale Project on the GCS share of the supercomputer JUQUEEN at Jülich Supercomputing Centre (JSC). GCS is the alliance of the three national supercomputing centres HLRS (Universität Stuttgart), JSC (Forschungszentrum Jülich), and LRZ (Bayerische Akademie der Wissenschaften), funded by the German Federal Ministry of Education and Research (BMBF) and the German State Ministries for Research of Baden-Württemberg (MWK), Bayern (StMWFK), and Nordrhein-Westfalen (MIWF).

APPENDIX A TEST OF STREAMING INSTABILITY

As we stated in Section 4.2, we expect the streaming instability to occur due to the achieved dust densities of $\varepsilon \geq 1.0$. However, with the resolution that we used, we do not resolve all possible modes. To make sure that the streaming instability that we see is accurate, we performed two tests. First, we simply doubled the numerical resolution so that smaller streaming modes are resolved. Second, we performed a test without a vortex and no radial stratification ($\beta = 0.0$), but increased the initial dust-to-gas ratio to a value where we were sure that streaming instability would be triggered. This way, we can make sure that the streaming instability, in general, can be seen with the resolution we use.

There was no significant difference between our standard resolution and the first test case (Figures 13 and 3, lower right). We see the same streaming structures in the particle density and the achieved overdensities in both cases are comparable.

Therefore, we can deduce that the standard resolution we used for all simulations is high enough to capture the essence of the streaming instability.

The second case also showed streaming structures (Figure 14). This shows that our resolution is high enough to show the streaming instability and that the streaming structures are not simply a result of particle accumulation in the vortex. The vortex accumulation first produces a high concentration of particles, but then the streaming instability kicks in to further increase the local dust-to-gas ratio.

REFERENCES

- Adams, F. C., & Watkins, R. 1995, *ApJ*, 451, 314
 Barge, P., & Sommeria, J. 1995, *A&A*, 295, L1
 Barranco, J. A., & Marcus, P. S. 2005, *ApJ*, 623, 1157
 Birnstiel, T., Dullemond, C. P., & Brauer, F. 2010, *A&A*, 513, A79
 Birnstiel, T., Klahr, H., & Ercolano, B. 2012, *A&A*, 539, A148
 Bottke, W. F., Durda, D. D., Nesvorný, D., et al. 2005, *Icar*, 179, 63
 Brauer, F., Dullemond, C. P., & Henning, T. 2008, *A&A*, 480, 859
 Chang, P., & Oishi, J. S. 2010, *ApJ*, 721, 1593
 Chavanis, P. H. 2000, *A&A*, 356, 1089
 Dittrich, K., Klahr, H., & Johansen, A. 2013, *ApJ*, 763, 117
 Dumusque, X., Pepe, F., Lovis, C., et al. 2012, *Natur*, 491, 207
 Goldreich, P., & Ward, W. R. 1973, *ApJ*, 183, 1051
 Güttler, C., Blum, J., Zsom, A., Ormel, C. W., & Dullemond, C. P. 2010, *A&A*, 513, A56
 Johansen, A., Andersen, A. C., & Brandenburg, A. 2004, *A&A*, 417, 361
 Johansen, A., Klahr, H., & Henning, T. 2006a, *ApJ*, 636, 1121
 Johansen, A., Klahr, H., & Henning, T. 2011, *A&A*, 529, A62
 Johansen, A., Klahr, H., & Mee, A. J. 2006b, *MNRAS*, 370, L71
 Johansen, A., Oishi, J. S., Mac Low, M.-M., et al. 2007, *Natur*, 448, 1022
 Johansen, A., & Youdin, A. 2007, *ApJ*, 662, 627
 Johansen, A., Youdin, A., & Mac Low, M.-M. 2009, *ApJL*, 704, L75
 Klahr, H., & Bodenheimer, P. 2006, *ApJ*, 639, 432
 Klahr, H. H., & Bodenheimer, P. 2003, *ApJ*, 582, 869
 Klahr, H. H., & Henning, T. 1997, *Icar*, 128, 213
 Klahr, H., & Hubbard, A. 2014, *ApJ*, 788, 21
 Klahr, H. H., & Lin, D. N. C. 2001, *ApJ*, 554, 1095
 Klahr, H. H., & Lin, D. N. C. 2005, *ApJ*, 632, 1113
 Lambrechts, M., & Johansen, A. 2012, *A&A*, 544, A32
 Lesur, G., & Papaloizou, J. C. B. 2009, *A&A*, 498, 1
 Lesur, G., & Papaloizou, J. C. B. 2010, *A&A*, 513, A60
 Lyra, W., Johansen, A., Klahr, H., & Piskunov, N. 2008a, *A&A*, 491, L41
 Lyra, W., Johansen, A., Klahr, H., & Piskunov, N. 2008b, *A&A*, 479, 883
 Lyra, W., Johansen, A., Klahr, H., & Piskunov, N. 2009a, *A&A*, 493, 1125
 Lyra, W., Johansen, A., Zsom, A., Klahr, H., & Piskunov, N. 2009b, *A&A*, 497, 869
 Lyra, W., & Klahr, H. 2011, *A&A*, 527, A138
 Lyra, W., & Lin, M.-K. 2013, *ApJ*, 775, 17
 Lyra, W. 2014, *ApJ*, 789, 77
 Meheut, H., Keppens, R., Casse, F., & Benz, W. 2012a, *A&A*, 542, A9
 Meheut, H., Meliani, Z., Varniere, P., & Benz, W. 2012b, *A&A*, 545, A134
 Morbidelli, A., Bottke, W. F., Nesvorný, D., & Levison, H. F. 2009, *Icar*, 204, 558
 Mordasini, C., Alibert, Y., Benz, W., Klahr, H., & Henning, T. 2012, *A&A*, 541, A97
 Nakagawa, Y., Sekiya, M., & Hayashi, C. 1986, *Icar*, 67, 375
 Nesvorný, D., Vokrouhlický, D., Bottke, W. F., Noll, K., & Levison, H. F. 2011, *AJ*, 141, 159
 Niedzielski, A., Nowak, G., Adamów, M., & Wolszczan, A. 2009, *ApJ*, 707, 768
 Okuzumi, S., Tanaka, H., Takeuchi, T., & Sakagami, M.-a. 2011a, *ApJ*, 731, 95
 Okuzumi, S., Tanaka, H., Takeuchi, T., & Sakagami, M.-a. 2011b, *ApJ*, 731, 96
 Ormel, C. W., & Cuzzi, J. N. 2007, *A&A*, 466, 413
 Petersen, M. R., Julien, K., & Stewart, G. R. 2007a, *ApJ*, 658, 1236
 Petersen, M. R., Stewart, G. R., & Julien, K. 2007b, *ApJ*, 658, 1252
 Raettig, N., Lyra, W., & Klahr, H. 2013, *ApJ*, 765, 115
 Safronov, V. S. 1972, *Evolution of the Protoplanetary Cloud and Formation of the Earth and Planets* (Jerusalem: Keter)
 Shakura, N. I., & Sunyaev, R. A. 1973, *A&A*, 24, 337
 Tanga, P., Babiano, A., Dubrulle, B., & Provenzale, A. 1996, *Icar*, 121, 158

- van der Marel, N., van Dishoek, E. F., Bruderer, S., et al. 2013, [Sci](#), **340**, 1199
- Weidenschilling, S. J. 1977, [MNRAS](#), **180**, 57
- Weidenschilling, S. J. 2011, [Icar](#), **214**, 671
- Weidenschilling, S. J., & Cuzzi, J. N. 1993, in Protostars and Planets III, ed. E. H. Levy, & J. I. Lunine, 1031
- Whipple, F. L. 1972, in From Plasma to Planet, ed. A. Elvius, 211
- Wolf, S., & Klahr, H. 2002, [ApJL](#), **578**, L79
- Wurm, G., & Blum, J. 2000, [ApJL](#), **529**, L57
- Youdin, A., & Johansen, A. 2007, [ApJ](#), **662**, 613
- Youdin, A. N., & Goodman, J. 2005, [ApJ](#), **620**, 459
- Zsom, A., Ormel, C. W., Güttler, C., Blum, J., & Dullemond, C. P. 2010, [A&A](#), **513**, A57